Article

A

Immobilized *p*-Sulfonic Acid Calix[4]Arene on Silica for Glycerol Acetalization: Influence of Preparation Method on Catalyst Microstructure and Catalytic Properties

Carlos Henrique C. Zacchi,[a,b] *Sara S. Vieira,* [*,a,c] *José D. Ardisson,*[d] *Ângelo de Fátima* [*,a]
and Maria Helena Araujo [*,a]

[a]Departamento de Química, Instituto de Ciências Exatas, Universidade Federal de Minas Gerais, 31270-901 Belo Horizonte-MG, Brazil

[b]Departamento de Química, Centro Federal de Educação Tecnológica de Minas Gerais, 30421-169 Belo Horizonte-MG, Brazil

[c]Departamento de Química Inorgânica, Instituto de Química, Universidade Federal Fluminense, 24020-141 Niterói-RJ, Brazil

[d]Laboratório de Física Aplicada, Centro de Desenvolvimento da Tecnologia Nuclear, 30123-970 Belo Horizonte-MG, Brazil

In this investigation, we synthesized magnetic nanoparticles coated with silica and functionalized with *p*-sulfonic acid calix[4]arene (CX4), to be used as heterogeneous acid catalysts for acetal synthesis. We evaluated the catalytic efficiency of these nanoparticles for acetal synthesis using various aldehydes and glycerol under microwave irradiation at atmospheric pressure, with and without solvents. Two distinct synthesis methods, Pechini (Fe/pch/Si/CX4) and precipitation (Fe/ppt/Si/CX4), resulted in variations in the physical and chemical properties of the solids produced. Structural characterization involved thermogravimetry analysis (TG), X-ray diffraction (XRD), Mössbauer spectroscopy, vibrating sample magnetometry, scanning and transmission electron microscopy (SEM and TEM), infrared spectroscopy (FTIR), and titration for acidic site quantification. Fe/ppt/Si/CX4 exhibited goethite phases, while Fe/pch/Si/CX4 showed a substantial proportion of maghemite. Both catalysts demonstrated significant activity in acetal synthesis, achieving approximately 80% conversion without solvents. Notably, Fe/ppt/Si/CX4 exhibited higher activity likely due to its structural properties and crystalline phases of the synthesized iron oxide, suggesting a composition difference from the Pechini method.

Keywords: magnetic nano catalyst, heterogeneous catalyst, *p*-sulfonic acid calix[4]arene, green chemistry, acetalization

Introduction

Glycerol is the main co-product obtained from the transesterification of triglycerides to produce biodiesel. However, the volume produced is large, and the market does not fully absorb the excess. Therefore, exploring alternatives to transform this molecule into higher value-added products is essential. [1-8] Among the catalytic routes that seek to chemically transform the glycerol molecule are hydrogenolysis,[9,10] dehydration,[11-14] oxidation,[4,15] steam reforming,[16,17] esterification,[18,19] etherification,[20,21] ketalization,[22] and acetalization.[5,7,23-28]

Acetals are substances obtained from a reversible reaction between polyalcohols (such as glycerol) and aldehydes or ketones, in the presence of an acid catalyst. Acetals derived from glycerol have several applications, including fuel additives (used as antifreeze substances for biodiesel),[29] surfactants,[30] and flavorings.[31]

The acetalization process of glycerol occurs in a dual-phase manner, initially generating a hemiacetal that undergoes intramolecular cyclization involving one of the remaining hydroxyl groups. This progression results in the formation of the acetal. The overall acetalization of glycerol typically yields an equimolar combination of five- and six-membered acetals. This outcome is attributed, in part, to the comparable reactivity exhibited by the primary and secondary hydroxyl groups.[32] Additionally, each isomer has

*e-mail: mharaujo@ufmg.br; adefatima@ufmg.br, adefatima.geqob@gmail.com; sarasilveira@id.uff.br

the *cis* and *trans* stereoisomers (except when the aldehyde used is formaldehyde); thus, four different isomers of acetal may be formed in the reaction mixture (Figure 1).[8]
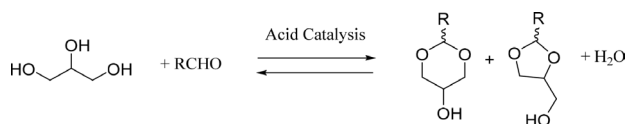

Figure 1. General scheme of the synthesis of acetals from glycerol and aldehyde. R = (hetero)aromatic or alkyl groups.

Several reports describe the use of heterogeneous materials bearing interesting catalytic properties for the acetalization of glycerol, such as ion exchange resins, zeolites,[22,26,33] montmorillonite, and bentonite,[34,35] metal oxides,[27,28,36] activated carbon,[37] mesoporous silica,[24,38] and ionic liquids.[35,39]

Due to their exceptional magnetic, electrical, physicochemical, and morphological properties,[40,41] iron oxides such as hematite (α-Fe$_2$O$_3$), goethite (α-FeOOH), maghemite (γ-Fe$_2$O$_3$), and magnetite (Fe$_3$O$_4$), have been widely used in various research and technological applications involving heterogeneous catalysis, demonstrating effective catalytic performance. Their appeal lies not only in their effectiveness but also in their ability to act as both catalysts and supports. They can be readily recovered and reused in subsequent reaction cycles without significant activity loss due to their magnetic properties. However, a substantial challenge in using iron oxides in heterogeneous catalysis is their tendency for particle aggregation, which can impair catalytic performance.[42] To overcome these limitations like oxidation, corrosion, and aggregation,[43] metallic nanoparticles (MNPs) can be coated with silica (SiO$_2$). This silica coating increases particle stability, ensuring its integrity and prolonging its lifespan. Additionally, it provides a tailorable surface, allowing for the incorporation of specific molecules that impart desired properties or functionalities to the material, thereby enhancing catalytic efficiency and selectivity.[44-46]

Calixarenes are macrocyclic compounds synthesized from the *ortho*-condensation of substituted phenols and formaldehyde in the presence of inorganic bases. Their appeal as catalysts stems partly from their ease and affordability of preparation, their versatility in functionalization, the ability to incorporate chirality, and the presence of multiple binding sites. These properties facilitate the creation of heterogeneous catalysts.[47,48] Easily modified functional groups on these calixarenes allow them to bind to solid supports like silica. Once immobilized, calixarenes can act as catalytic centers in various reactions, such as synthesizing acetals from glycerol and aldehyde. The acidity of calixarene-based systems can be tuned through a combination of factors, including specific functional groups, the structure of the molecule, interactions within its hydrophobic cavity, and the reaction environment.[49,50]

The presence of SO$_3$H groups (sulfonic acid) in calixarenes significantly enhances the acidity of this structure. When dissolved, these calixarenes readily release a proton from the sulfonic acid group, forming hydronium ions (H$_3$O$^+$), thereby increasing the acidity of the solution. Additionally, the SO$_3$H group can stabilize through resonance, facilitating further proton donation and augmenting the acidity of the group.[51,52]

In this study, to investigate how the preparation method affects the catalytic properties of magnetic nanoparticles (MNPs) (Figure 2), we synthesized MNPs using both the Pechini (pch) and precipitation (ppt) methods. The Pechini method yields highly pure polycrystalline materials with nanoscale particle sizes.[53,54] In contrast, nanoparticles produced by the controlled precipitation method often exhibit lower size uniformity. However, this method is widely used for its simplicity and productivity.[47,53-56]

The MNPs were then coated with silica and functionalized with calixarenes. Notably, *p*-sulfonic acid calix[4]arene (CX4) has not been extensively explored as a catalyst for glycerol acetal formation in existing literature. Therefore, in addition to evaluating the effectiveness of this catalyst in a homogeneous medium, our study explores its application when supported on the surface of silica-coated iron oxides, creating a heterogeneous, acid-functionalized magnetic catalyst.

Experimental

Synthesis and characterization of the MNPs

Synthesis of MNPs by Pechini method (Fe/pch)

To obtain iron nanoparticles using the Pechini method (Fe/pch), a combination of iron(III) chloride hexahydrate (FeCl$_3$·6H$_2$O), citric acid ((HOC(COOH)(CH$_2$COOH)$_2$)), (citric acid/metal molar ratio: 3/1), and ethylene glycol (HOCH$_2$CH$_2$OH) (citric acid/ethylene glycol mass ratio: 60/40) was employed. FeCl$_3$.6H$_2$O was dissolved in an aqueous citric acid solution followed by homogenization (to ensure uniform mixing) and stirred at 60 °C for 30 min. Then, the addition of ethylene glycol initiated the polymerization process. The solution was continuously stirred and heated at 120 °C for approximately 90 min after adding ethylene glycol. Once a high viscosity was reached, the obtained resin was transferred to a muffle furnace and
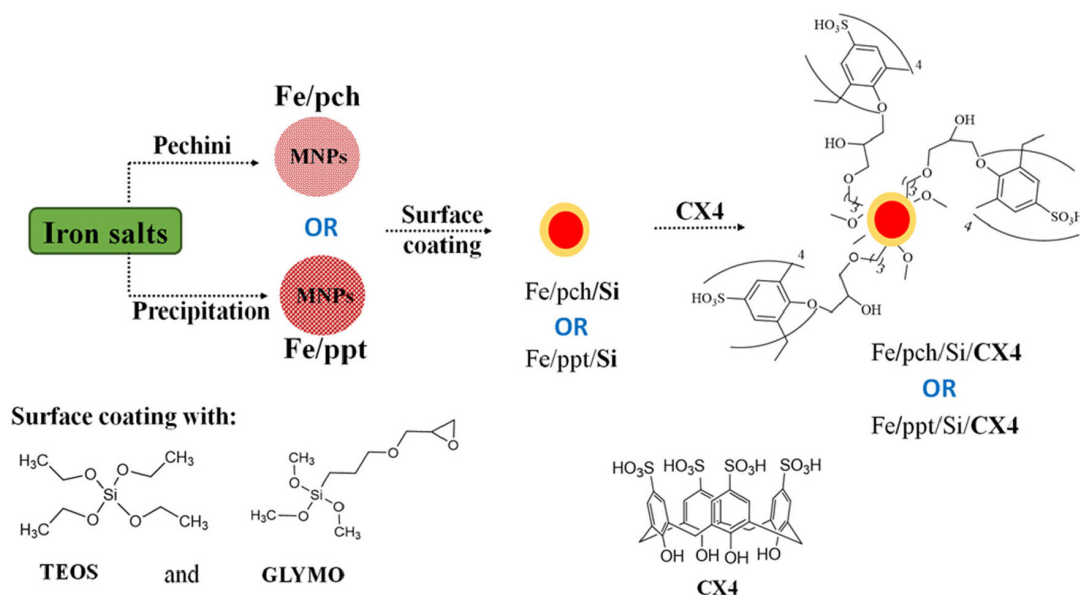
Figure 2. The preparation scheme for the magnetic catalysts outlines the pathways for synthesizing $Fe_3O_4/ppt/SiO_2/CX4$ and $Fe_3O_4/pch/SiO_2/CX4$.

calcined at 300 °C (heating rate: 1 °C min^{-1}) for four hours to remove organic components. The resulting amorphous powder was de-agglomerated and further treated thermally under a N_2/H_2 atmosphere (with 10% H_2 at 50 mL min^{-1}) at 450 °C (heating rate: 2 °C min^{-1}) for two hours to crystallize the magnetic nanoparticles.[57,58]

Synthesis of MNPs by controlled precipitation method (Fe/ppt)

Fe/ppt MNPs were obtained by the controlled precipitation of iron(III) sulfate heptahydrate (100 mL of 0.1 mol L^{-1} $FeSO_4.7H_2O$) using sodium hydroxide solution (0.45 mol L^{-1} NaOH),which was added dropwise until the solution reached pH 12 (to induce precipitation of iron nanoparticles). The brown solid was filtered, washed (50 mL of H_2O), and oven-dried at 50 °C for 24 h.[47,59]

Silica-coated MNPs (Fe/pch/Si or Fe/ppt/Si)

Magnetic nanoparticles were modified using a previously published method.[60] Typically, 0.5 g of the nanoparticles were suspended in a mixture of 25 mL distilled water, 3.75 mL of methanol (CH_3OH), sodium fluoride (1.25 mL of a 1% water solution of NaF), and 1.35 mL of 3-glycidoxypropyl-trimethoxy-silane (GLYMO). The mixture was stirred for 15 min at room temperature. Subsequently, 7.5 mL of tetraethyl orthosilicate (TEOS) were then slowly added dropwise to the mixture, which continued stirring for 48 h at room temperature. The resulting material was separated using magnetic methods, washed with water and ethanol until a neutral pH was achieved, and dried in an oven at 50 °C for 24 h.

Immobilization of *p*-sulfonic acid calix[4]arene (CX4) on MNPs coated with silica

Initially, CX4 was synthesized by combining 3.5 mmol *p-tert*-butylcalix[4]arene and 15 mL of concentrated sulfuric acid (H_2SO_4), stirring continuously for 4 h at 80 °C. The resulting black solid was filtered, washed with 200 mL of ethyl acetate ($CH_3COOC_2H_5$), and oven-dried at 50 °C for 24 h.[47,61,62]

The methodology proposed by Sayin *et al.*[63] was followed to integrate CX4 into the silica-coated magnetic nanoparticles (MNPs). In this process, 0.15 g of CX4 and 0.112 g of potassium carbonate (K_2CO_3) were stirred in 10 mL of acetonitrile (CH_3CN) for 30 min at room temperature. Subsequently, 0.45 g of MNPs were added, and the mixture was refluxed for 72 h. The resulting mixture was acidified with 2 mL of a 0.1 mol L^{-1} HCl solution. The obtained solids were separated magnetically and washed with water and ethanol (approximately 20 mL each) until a neutral pH was achieved. Finally, the materials were oven-dried at 50 °C for 24 h.

Characterization of the catalysts

The catalysts were characterized by thermal analysis in a DTG-60 Shimadzu instrument (Osaka, Japan) under nitrogen flow (50 mL min^{-1}) range of 30-1000 °C at a heating rate of 10 °C min^{-1}. X-ray diffraction was performed in a Rigaku Geigerflex model (Tokyo, Japan) using Cu Kα radiation (1.5406 Å) with a scanning speed of 2° min^{-1}. Scherrer's equation estimated the average crystallite sizes. Mössbauer analyses were performed using a conventional CMTE-MA250 spectrometer (Starnberg, Germany) with constant acceleration by moving a ^{57}Co source into an Rh

J. Braz. Chem. Soc. **2024**, *35*, 11, e-20240076

3 of 14

matrix to identify the phases of iron-containing materials. Magnetization hysteresis loops were measured at room temperature using a LakeShore Model 7404 (Westerville, United States) vibrating sample magnetometer (VSM), with a time constant of 100 ms and 400 Oe s⁻¹ sweep rate.

The specific surface areas of the samples were analyzed by Brunauer-Emmett-Teller (BET) adsorption of N_2 at 77 K using an Autosorb1-MP Quantachrome instrument (Kyoto, Japan). The samples were degassed at 200 °C for 24 h before analysis. For the titration of acidic sites, 20 mg of the sample was dispersed in 20 mL of a KOH solution (0.02 mol L⁻¹). After reaching equilibrium (4 h), the solution was filtered and titrated with 0.02 mol L⁻¹ HCl. All solutions were standardized, and the analyses were performed in triplicate. The Fourier transform infrared spectra (FTIR) of the materials (in the form of KBr pellets) were measured using a PerkinElmer FTIR GX spectrometer (São Paulo, Brazil) in the range of 400-4000 cm⁻¹ at a resolution of 4 cm⁻¹.

The morphological characterization of the material was carried out by scanning electron microscopy (SEM) on Quanta 200-FEG 3D-FEI equipment (Billerica, USA). Transmission electron microscopy (TEM) images were obtained in a Tecnai G2-20-SuperTwin FEI-200 kV transmission electron microscope (Oregon, United States). The powder samples were dispersed in acetone and deposited on a copper-coated grid.

Catalytic tests: synthesis of the glycerol acetals

Microwave-assisted synthesis was employed for the catalytic tests. In each experiment, 1.0 mmol of the chosen aldehyde, 1.0 mmol of glycerol, and 50.0 mg of the catalyst (either Fe/ppt/Si/CX4 or Fe/pch/Si/CX4) were transferred to a microwave reactor (CEM Discovery System, Model 908005, East Lyme, United States) operating at 50/60 Hz with a maximum power of 250 W and a microwave frequency of 2455 MHz. The reaction mixture was maintained in the microwave reactor under atmospheric pressure for 10 min at 100 °C. The reactions were carried out in the absence of solvent and in the presence of methanol, ethanol, dimethyl sulfoxide (DMSO), and toluene.

After the reaction, the obtained mixture was solubilized in ethanol (2 mL), and the catalyst was removed with a magnet, washed with ethanol, and dried in an oven at 50 °C for reuse. Following catalyst removal, the ethanol was evaporated, and the reaction mixture was dissolved in ethyl acetate and filtered using a short silica column with ethyl acetate as eluent. The reaction yielded a mixture of five- and six-membered isomers, which were characterized by ¹H nuclear magnetic resonance (NMR) spectroscopy (using a Bruker DPX 400 Avance spectrophotometer Ettlingen,

Germany operating at 400 MHz) to quantify the percentage of each isomer in the mixture. The NMR data for the five- and six-membered isomers of **3a-3e** were referenced from previously published work by Castro *et al.*[50]

Results and Discussion

Synthesis and characterization of the catalysts

Magnetic catalysts coated with silica and modified with *p*-sulfonic acid calix[4]arene (CX4) represent a remarkable technological innovation with broad potential across various domains due to their unique properties and synergistic interaction among their distinct components. These structures stand out for their ability to precisely control structure and composition, allowing for adjusting their catalytic and magnetic properties to meet specific needs. This includes optimizing the size, shape, distribution, and concentration of acid groups and magnetic particles within the silica matrix, aiming to maximize both catalytic activity and efficient recovery of the catalyst.

At its core, the fundamental technological innovation of magnetic catalysts coated with silica and modified with acid groups lies in the ability to design multifunctional materials with tailored properties for specific applications. This capability of tailored design offers a practical, versatile, and sustainable solution for various chemical and environmental processes.

Producing materials with well-defined structures and controlled morphologies is a significant challenge in materials science. This is because the size and shape of nanoparticles directly influence their performance in heterogeneous catalysis reactions as they will determine the availability of active sites present on the surface, which may affect the intensity of the bond between the reactant/catalyst/product and, thus, the activity and catalytic selectivity for a particular reaction.[64,65]

In this study, we sought to evaluate the influence of the synthesis methodology used to prepare magnetic iron oxides on their performance in acetalization reactions for glycerol valorization. The magnetic materials were obtained from two methodologies, Pechini (Fe/pch) and controlled precipitation (Fe/ppt) and characterized before being coated with silica. Then, the homogeneous catalyst, CX4, was supported on the nanoparticles (Figure 2). As previously reported by our group,[47,66,67] CX4 can be used effectively in both homogeneous and heterogeneous media for various organic reactions. The characterization of CX4 has been reported in our previous studies.[47]

The Fe/ppt catalyst used in this study has been previously characterized and documented by our group.[47]

Here, we present the characterization data for the Fe/pch catalyst. We will then compare the properties of both catalysts to evaluate the influence of the preparation method.

From the thermogravimetric analysis (TGA) data, the Fe/ppt material loses around 4% of its original mass, between 80-320 °C, attributed to water molecules in the structure.[47] The Fe/pch (Figure 3) loses around 17% of its original mass between 75-440 °C, likely due to the presence of water molecules and organic matter present in the structure.[68,69] This mass loss can also be attributed to the thermal transformation of the iron oxide crystal structure from magnetite (Fe_3O_4) to maghemite (γ-Fe_2O_3) occurring between 300 and 440 °C.[40] Furthermore, differential thermal analysis (DTA) analysis allows us to observe a peak centered at 370 °C, associated with the oxidation of residual organic compounds and the transformation of crystalline phases.
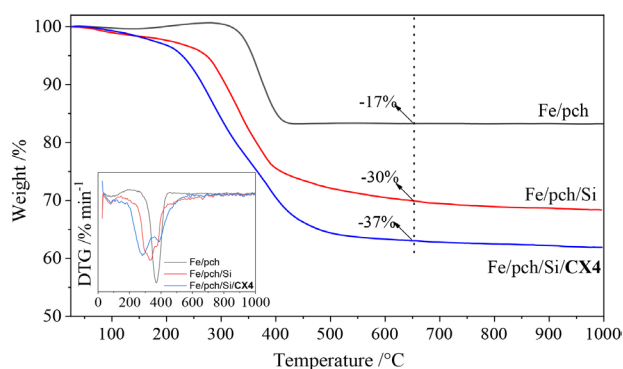

Figure 3. TGA and DTA (insert) curves of Fe/pch/Si/CX4 at a heating rate of 10 °C min^{-1} in an N_2 atmosphere.

TGA provides another critical piece of information: the amount of silica incorporated into the MNPs. The mass loss, which was 19 and 13%, for Fe/ppt/Si (observed between 70-650 °C) and Fe/pch/Si (between 65-650 °C), respectively, is attributed to water molecules and mainly the decomposition of residual GLYMO and TEOS groups introduced during the incorporation of silica particles onto the MNPs. TGA also indicates that ca. 6 and 7% of CX4 were supported on the surface of the silica-coated MNPs, producing Fe/ppt/Si/CX4 (observed between 70-650 °C) and Fe/pch/Si/CX4 (observed between 65-650 °C) respectively. The DTG curve for Fe/ppt/Si/CX4 is relatively narrow and shifted to higher temperatures (368 and 447 °C). This may indicate that the CX4 is anchored on more homogeneous, stable, and organized silica-coated magnetic nanoparticles.

The concentration of the acid sites was determined by titration as described in Zacchi *et al.*[47] According to the data presented in Table 1, the silica-coated magnetic

nanoparticles increase the total acid site concentration. This can be attributed to the presence of silanol groups (−SiOH) on the silica surface, which contribute to the overall acidity of the material,[50] and to the potential interaction between MNPs and SiO_2 that may modify the electronic structure of the material, making it more favorable for proton donation.

Adding the *p*-sulfonic-calix[4]arene acid (CX4) groups significantly increases the acidity of the silica-coated magnetic nanoparticle catalysts. For Fe/ppt/Si/CX4 and Fe/pch/Si/CX4, the concentration of acid groups was 0.70 and 0.75 mmol H$^+$ g^{-1}, respectively (Table 1). This increase is primarily due to the presence of sulfonic groups, which are strong proton donors, increasing the total acidity of the catalyst. Additionally, hydroxyl groups within the structure can also donate protons, contributing to the overall acidity.[70] The slight difference observed between the Fe/ppt/Si/CX4 and Fe/pch/Si/CX4 values may be related to the efficiency of anchoring CX4 groups to the catalysts, resulting in variations in the concentration of acidic protons.

Table 1. The concentration of acid sites, BET area (S$_{BET}$), and calculated crystallite diameter (D$_{311}$) for the materials

Material	Acid site / (mmol H$^+$ g^{-1})	S$_{BET}$ / (m^2 g^{-1})	D$_{311}$ / nm
Fe/pch	0.22	22	17
Fe/pch/Si	0.35	–	–
Fe/pch/Si/CX4	0.75	17	16
Fe/ppt	0.23	20	17
Fe/ppt/Si	0.35	–	–
Fe/ppt/Si/CX4	0.70	14	15

pch: Pechini; ppt: precipitation; CX4: *p*-sulfonic acid calix[4]arene.

The X-ray diffraction (XRD) analysis provided valuable insights into the crystalline structure and phase variations of the nano catalyst synthesized from silica incorporated with magnetic iron oxide and modified with *p*-sulfonic acid calix[4]arene. The presence of distinct iron oxide phases, Fe_3O_4 (JCPD-19-629) and γ-Fe_2O_3 (JCPD-39-1346) was confirmed by the diffraction peaks observed in the samples, consistent with the Joint Committee on Powder Diffraction Standards (JCPDS).

Interestingly, additional phases were also identified in specific samples. For instance, the presence of α-FeOOH (JCPD-29-713) and FeO (JCPD-6-696) was observed in the Fe/ppt and Fe/pch samples, respectively, as depicted in Figure 4. This suggests that the synthesis methodology may have influenced the formation of these secondary phases, indicating variations in the reaction conditions or precursor compositions.
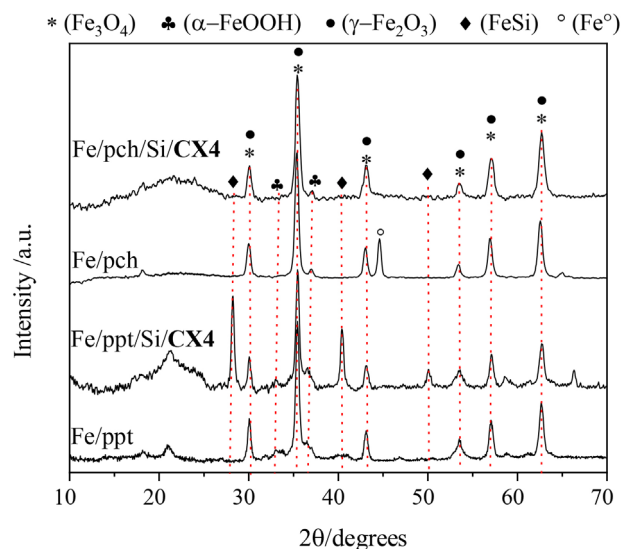
J. Braz. Chem. Soc. **2024**, *35*, 11, e-20240076

5 of 14

Figure 4. Powder XRD pattern of the iron oxides prepared by different methodologies and after the silanization/CX4 reactions.

Despite the presence of additional phases, it is noteworthy that the intensity and width of the diffraction peaks among the various synthesized iron oxides did not significantly alter. This indicates that the silanization and functionalization processes did not induce significant changes in the overall crystalline structure of the nanomaterials.

However, a slight loss of crystallinity was noted, along with the appearance of an extra peak at approximately 22°, which can be attributed to the formation of an amorphous silica shell around the magnetic nanoparticle (MNP) core. This amorphous silica layer was further confirmed by a broad peak observed at 20-28°, consistent with the characteristic amorphous structure of silica.

In summary, the XRD analysis revealed the presence of various iron oxide phases and confirmed the formation of an amorphous silica shell around the magnetic nanoparticle core. These findings provide important insights into the synthesized nano catalyst's structural characteristics and phase variations, which are crucial for understanding its catalytic behavior and potential applications in various fields.[68,71]

As we have already seen from the XRD data (Figure 4), the Fe_3O_4 and γ-Fe_2O_3 phases have very similar diffraction patterns. The three-dimensional structure of Fe_3O_4 and γ-Fe_2O_3 phases, shown in Figure 5, were obtained from the Crystallographic Information File (CIF) taken from the Crystallography Open Database and generated from Vesta (Visualization software for Electronic and Structure Analysis).[72,73]

Fe_3O_4 is an inverse spinel with a face-centered cubic unit cell based on O^{2-} ions that are regularly cubic close-packed along the plane [111]. It also features tetrahedral sites occupied by Fe^{3+} ions, while octahedral sites are occupied by both Fe^{2+} and Fe^{3+} ions. γ-Fe_2O_3 has a similar structure to magnetite but contains only Fe^{3+} ions, with cation vacancies compensating for the oxidation of Fe^{2+}. Each unit cell contains 32 O^{2-} ions, 21 Fe^{3+} ions, and two vacancies. Eight cations are situated in tetrahedral sites, with the remaining cations randomly dispersed across octahedral sites.[74] As detailed by Teixeira *et al.*,[40] magnetite exhibits the inverted magnetic spinel structure, featuring Fe^{2+} as a crucial electron donor. The authors further emphasize that the octahedral site in this structure can readily host both Fe^{2+} and Fe^{3+}, leading to fascinating redox chemistry within the solid framework. Moreover, within this structure, the complete oxidation of Fe^{2+} transforms magnetite into magnetic maghemite (γ-Fe_2O_3), maintaining the same spinel structure.

Scherrer equation analysis using the D_{311} plane revealed no significant variation in the average crystallite size for the samples (Table 1). Similarly, the BET surface area values (Table 1) also showed no significant changes. This suggests that the incorporation of SiO_2 did not lead to the agglomeration of MNPs, preserving their original crystallite size. Furthermore, the presence of SiO_2 might have stabilized defects or nucleation sites within the MNP structure, hindering crystallite growth.
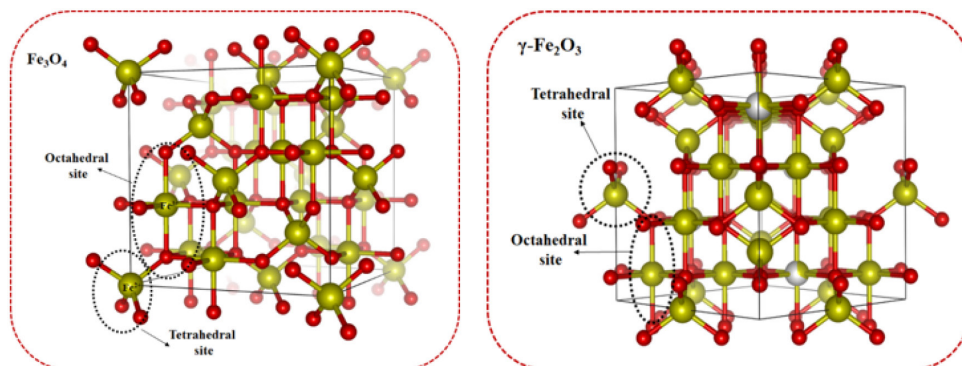

Figure 5. Three-dimensional structure of the phases Fe_3O_4 and γ-Fe_2O_3. All structures were generated from the Crystallographic Information File (CIF),[72,73] taken from the Crystallography Open Database, and from Vesta (Visualization software for Electronic and Structure Analysis).

The low BET surface area observed can be attributed to a combination of factors specific to the synthesis methodologies used. For Fe/ppt, factors like uncontrolled crystallite growth, particle agglomeration, and synthesis parameters (pH, temperature, reagent addition rate, and reaction time) might have contributed to the low surface area.[75] This consequently limited the porosity of the structure, resulting in a practically non-existent pore network. For Fe/pch, the low BET surface area can likely be attributed to the chosen synthesis conditions, particularly the temperature and time used during the polymerization and subsequent carbonization steps. Additionally, particle agglomeration of iron oxide might have occurred during these thermal treatments, further reducing the surface area.

Mössbauer spectroscopy is a powerful technique that, combined with XRD results, provides complementary and detailed information about the structure and composition of materials containing iron oxides. This combined approach is particularly useful for materials exhibiting magnetite and maghemite phases. As shown in Figure 4, the XRD data suggests the presence of Fe_3O_4 and/or γ-Fe_2O_3 phases in the catalysts. However, XRD cannot distinguish between these two phases if they coexist. Mössbauer spectroscopy overcomes this limitation and provides information about the quantity of each phase present in the materials.

The Mössbauer spectra obtained showed that Fe/ppt is mainly composed of α-FeOOH, γ-Fe_2O_3, and Fe_3O_4, while Fe/pch primarily consists of Fe_3O_4 (Figure S1, Supplementary Information (SI) section). Interestingly, α-FeOOH phases were only observed in samples obtained from the controlled precipitation synthesis. According to Zacchi *et al.*,[47] ferrous sulfate dissociates and partially hydrolyzes to α-FeOOH in the presence of atmospheric oxygen during this type of synthesis.

Mössbauer spectroscopy revealed that the Fe_3O_4 phase (13% tetrahedral and 19% octahedral sites) represents 32% of the material obtained during controlled precipitation synthesis. Additionally, γ-Fe_2O_3 makes up 31% and α-FeOOH 28% of the structure. The addition of SiO_2 and CX4 decreased these percentages to 20, 9, and 24%, respectively. In the Pechini method, Fe_3O_4 was the primary phase, with 35% occupancy of tetrahedral sites and 38% occupancy of octahedral sites. No γ-Fe_2O_3 or α-FeOOH was detected by Mössbauer spectroscopy. However, incorporating silica and CX4 caused the oxidation of Fe^{2+} in Fe_3O_4, resulting in the formation of γ-Fe_2O_3 (70%) and a reduction in the percentages of Fe_3O_4. This transformation likely occurs because maghemite (γ-Fe_2O_3), which is more stable than magnetite (Fe_3O_4), forms due to interactions between SiO_2 and Fe_3O_4. These interactions

may induce favorable structural rearrangements that promote maghemite formation. Additionally, the presence of SiO_2 might stabilize defects or nucleation sites within the Fe_3O_4 structure, further favoring the transformation into maghemite during crystal growth.[76]

The magnetization was measured by sweeping the external field between ca. 8 kOe and 78.3 emu g^{-1} (Figure S2, SI section). The literature[76-78] reports that magnetic properties strongly depend on grain size and structure. This is reflected in the observed small hysteresis loops with remaining magnetization (5.4 and 5.7 emu g^{-1}) and coercivity (−90 and −470 Oe) for Fe/ppt and Fe/pch, respectively. The remaining magnetization (Mr) decreases upon modification of the structure with silica and CX4. These results, along with the findings of Rostami *et al.*[79] and Rajabzadeh *et al.*,[80] indicate the formation of a silica layer around the Fe_3O_4 nanoparticles.

Spectroscopy analysis in the infrared region reveals different bands corresponding to the structural characteristics of the Fe/ppt/Si/CX4 and Fe/pch/Si/CX4 (Figure S3, SI section). The stretching and deformation vibrations of the Fe−O bond at 560 cm^{-1} are associated with the octahedral and tetrahedral sites of the Fe_3O_4 structure.[81-83] The Fe−O vibration at 635 cm^{-1} indicates the presence of γ-Fe_2O_3.[84]

The process of coating iron oxide nanoparticles with silica (SiO_2) occurs by hydrolysis of the silica source. This hydrolysis process is evidenced by specific bands at 1180 and 900 cm^{-1}, corresponding to the Si−O−Si bond's symmetric and asymmetric stretching vibrations. The silanol groups (Si−OH) are identified in the 2800-3700 cm^{-1} region.[85-87]

The presence of the CX4 groups is confirmed by the characteristic bands corresponding to the aromatic rings at 1642 and 1452 cm^{-1}, representing the stretching vibrations of the aromatic C=C bonds of the calix[*n*]arene derivatives.[49] Furthermore, vibrations related to the S−O bond derived from *p*-sulfonic acid-calix[4]arene groups are observed at 1040 and 790 cm^{-1}. The vibrations of the O=S=O bond of the C−SO$_3$ group are detected in the region of 1080 cm^{-1}.[63,88-92]

The morphology, size, and microstructure of the various synthesized iron oxides are depicted in Figure 6. Notably, the nanoparticles display irregular shapes with diverse morphologies, including rounded features and, for Fe/ppt, needle-like structures. Goethite, a hydrated iron oxide with a monoclinic crystal structure, is likely responsible for the needle-like morphology observed in Fe/ppt. Due to its molecular geometry and atomic arrangement, goethite molecules tend to organize themselves into elongated crystals.[93] In general, a variety of irregular structures of different sizes is observed.

J. Braz. Chem. Soc. **2024**, *35*, 11, e-20240076

7 of 14

Figure 6. SEM images of the magnetic nanoparticles prepared by Pechini (Fe/pch) and precipitation (Fe/ppt) methods.
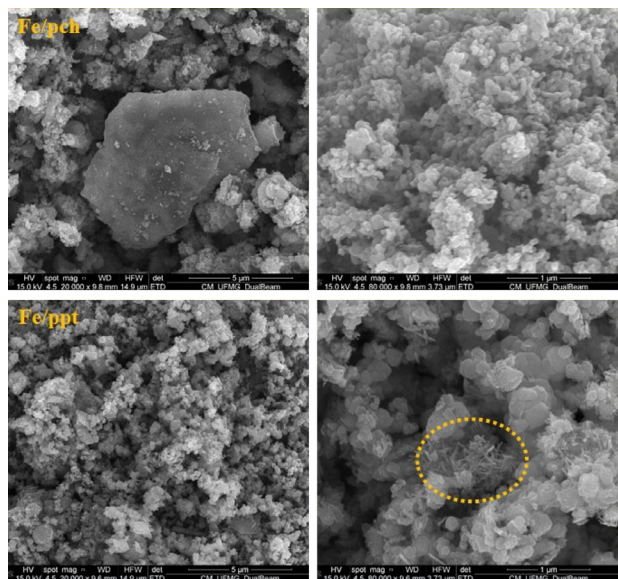

Figure 7. TEM images of the magnetic nanoparticles prepared by Pechini (Fe/pch) and precipitation (Fe/ppt) methods.

The employed synthesis methodology significantly influenced the shape and size of the MNPs, as observed in the obtained images. However, direct measurement of particle size distribution from these images was not possible. Existing literature suggests that MNPs obtained through controlled precipitation[59] typically results in particles with relatively uniform sizes, especially under meticulously controlled conditions. Conversely, the Pechini method[94] tends to yield iron oxide particles with a broader size distribution and less regular shapes due to the formation of a precursor polymeric gel that decomposes thermally to form the oxide. Surprisingly, our results (Figure 7) demonstrate the opposite. The images obtained indicate that the Pechini method produced MNPs with a more uniform size and shape. This discrepancy may be attributed to the abundance of needle-shaped particles observed, characteristic of goethite presence. The pattern of shape and size distribution was consistently observed for both the Fe/ppt/Si/CX4 and Fe/pch/Si/CX4 samples, as illustrated in the images in the Figure S4 (SI section).

Catalytic activity

This study investigated the conversion of glycerol to acetals using synthesized magnetic heterogeneous acid catalysts in the presence of different aldehydes. Microwave reactors were employed for these reactions. One of the main advantages of these reactors is their ability to reduce reaction time and precisely control parameters such as temperature. They allow for rapid and uniform heating, quickly reaching the desired reaction temperature. As a result, these s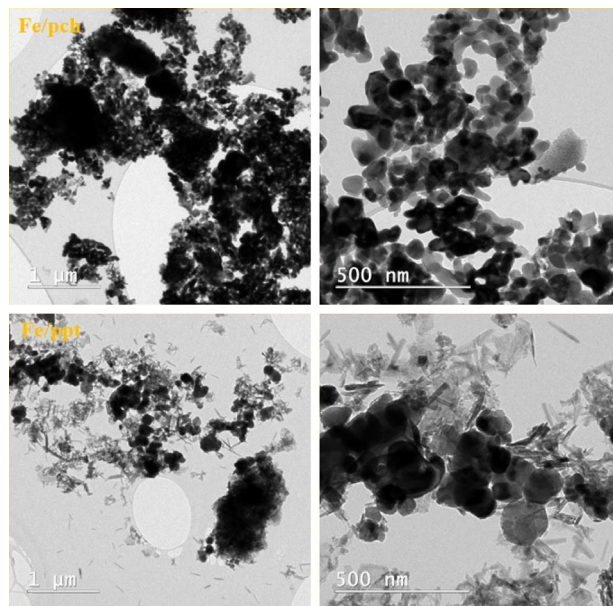ystems consume less energy compared to conventional methods. Additionally, reaction rates can increase significantly, leading to higher conversion and yield of reactants into desired products. This benefit is significant in temperature-sensitive reactions, such as acetalization, where precise temperature control is crucial to avoid decomposing reactants or forming unwanted by-products.[50]

Acetal formation relies on an acid catalyst, such as H_2SO_4, HF, HCl, and *p*-toluene sulfonic acid (PTSA).[1] In this reaction, the acid catalyst is crucial in initiating acetal formation. It activates the aldehyde, making the carbonyl group more reactive to nucleophilic attack initiated by glycerol's less hindered primary hydroxyl group. This is followed by a cyclization reaction, where water is expelled, and a simultaneous nucleophilic attack of the secondary or primary hydroxyl group occurs on the carbon-oxygen double bond. This process forms five- or six-membered rings, depending on the hydroxyl group involved.[95] The proposed mechanism for this reaction is illustrated in Figure 8.

According to the literature,[96] carbohydrates that are substrates similar to the intermediate formed in this reaction undergo preferential cyclization reactions after adding the carbonyl to form five- and six-membered rings, which are the kinetic and thermodynamic products, respectively. Mota *et al.*[97] reported that glycerol acetals follow the same principle of carbohydrate cyclization; the kinetically controlled product is the five-membered ring acetal, whereas the six-membered acetals are the thermodynamically controlled products.

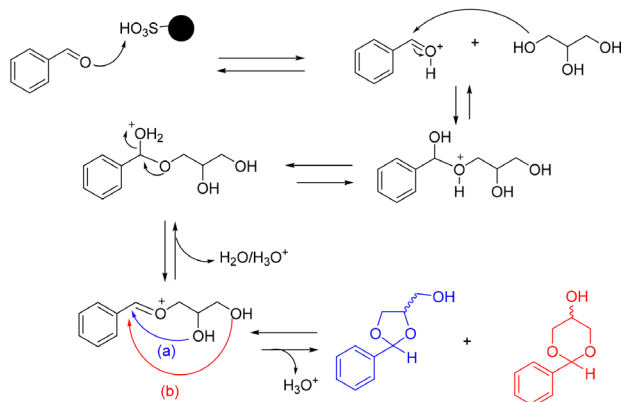In this work, the homogeneous catalyst *p*-sulfonic-

Figure 8. A proposed mechanism for obtaining five-membered (a) and six-membered (b) acetals from the reaction between benzaldehyde and glycerol.
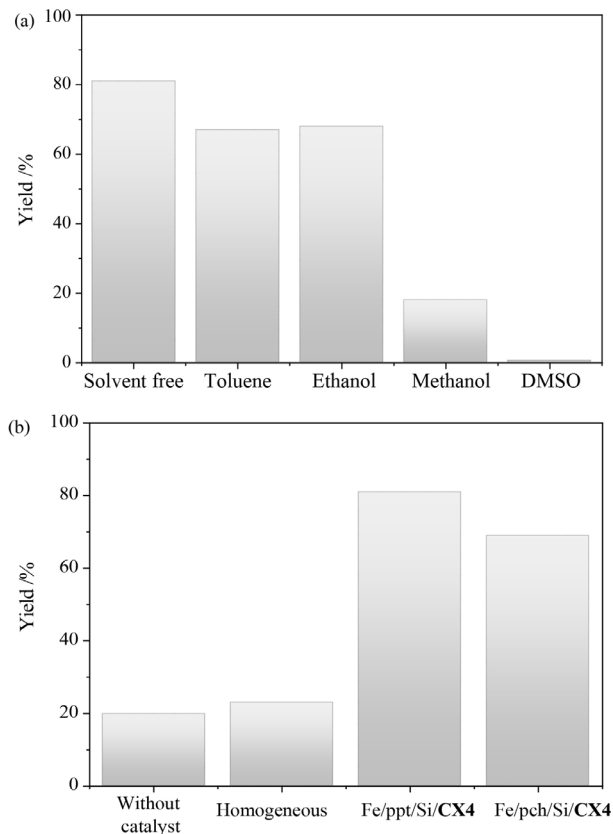

Figure 9. (a) Influence of the solvent on the benzaldehyde acetalization reaction using the Fe/ppt/Si/CX4 catalyst (reaction conditions: 100 ℃; MW, 10 min). (b) Influence of the catalyst on the benzaldehyde acetalization reaction (Reaction conditions: without solvent, 100 ℃; MW, 10 min).

calix[4]arene acid was supported on an inorganic magnetic matrix (composed of silica-coated MNPs), which facilitates the recovery of the catalyst so that it can be used again in other reaction cycles. The first stage of the work evaluated the influence of solvent polarity on the formation of acetals since they can affect the solubility of reactants, the stability of reaction intermediates, the equilibrium, and the kinetics of the reaction.

The reaction was carried out in the presence and absence of solvent using microwave irradiation (MW) heating. Protic solvents (methanol and ethanol) and DMSO, an aprotic solvent, were tested. Additionally, toluene was used because it can form an azeotrope with water. This can remove water from the system, shifting the reaction equilibrium to the acetal formation.

Based on the data from Figure 9a, a significant influence of solvent presence on the reaction yield is observed. While no product formation was observed in the presence of DMSO, the yield of acetals was higher when ethanol was used compared to methanol, as shown in Figure 9a. This difference in yield can be attributed to several factors, including the stability of intermediates formed during the reaction, the polarity, and the solubility of the solvent. Such conditions favor the formation of acetals in higher concentrations in the presence of ethanol.

As previously reported, the high yield observed in the presence of toluene can be explained by its ability to form an azeotropic mixture, removing water (a byproduct that can hinder the reaction). Additionally, the solvent-free reaction achieving a high yield (80% acetals) can be explained by the increased concentration of reactants due to the absence of solvent and potentially the formation of more reactive intermediates. Based on these results, we opted for a solvent-free approach for further studies.[50]

Figure 9b presents the yield of the benzaldehyde acetalization reaction using the synthesized Fe/ppt/Si/CX4

and Fe/pch/Si/CX4 catalysts, compared to a homogeneous CX4 catalyst and the uncatalyzed reaction. The results indicate that Fe/ppt/Si/CX4 and Fe/pch/Si/CX4 reactions achieved yields of 81 and 70%, respectively. A homogeneous CX4 catalyst resulted in a 25% yield, and the uncatalyzed reaction 20%.

The immobilization of *p*-sulfonic acid calix[4] arene (CX4) on silica-coated MNPs increases the availability of active sites accessible for the reaction. This combination can create synergy between properties, facilitating the activation of reagents[98] and promoting more efficient acetal formation. The synthesized heterogeneous catalysts can stabilize reaction intermediates, improving catalytic efficacy and increasing the overall reaction yield. This stabilization of intermediates may be related to modifying the polarity of the reaction medium through the interaction of reagents with the catalyst.

When comparing the reaction yield results for the two studied heterogeneous catalysts, it is observed that Fe/ppt/Si/CX4 (80.71%) was slightly more efficient than Fe/pch/Si/CX4 (71.85%). This difference is likely related to the type of crystal structure of the MNPs

formed. As observed by XRD (Figure 4) and Mössbauer spectroscopy data (Table S1 and Figure S1, SI section), α-FeOOH is present only in Fe/ppt/Si/CX4, while a high relative sub-spectral area for γ-Fe$_2$O$_3$ was observed in Fe/pch/Si/CX4. The presence of hydroxyl groups (OH$^-$) in the structure of α-FeOOH may facilitate the binding of CX4 through hydrogen bonding or other favorable chemical interactions. These functional groups on the goethite surface can provide more accessible and reactive binding sites for CX4 than maghemite's denser and less reactive structure. Additionally, as observed in the SEM images (Figure 6) and TEM images (Figure 7), these solids do not have homogeneous structures like those obtained by the Pechini method. The heterogeneity of the structure may also be one of the reasons for the improved catalytic activity of Fe/ppt/Si/CX4 compared to Fe/pch/Si/CX4.

To evaluate the influence of reaction variables (molar ratio, catalyst amount, and time) on reaction yield, assays were performed using Fe/ppt/Si/CX4 catalyst. The influence of catalyst content (Figure 10a) indicates that 0.064 mol% catalyst leads to higher yield. This result may indicate a maximum limit between the number of acid sites and the highest product yield. Similar results were obtained by da Silva *et al.*[66]

While not as efficient as the composite catalysts, Fe/ppt also demonstrates catalytic activity, achieving a 50% yield (Figure 10a). This activity is related to the chemical and crystalline structure of Fe/ppt, where α-FeOOH possesses hydroxyl groups that act as acidic centers, facilitating reagent activation. While less acidic, Fe$_3$O$_4$ and γ-Fe$_2$O$_3$ can still contribute to the reaction by stabilizing the reaction intermediates.[74]

Since the acetalization reaction is reversible, an excess of one reactant may drive the equilibrium towards product formation. Considering glycerol as the most readily available reagent, we investigated the effect of its molar ratio on the reaction yield (insert in Figure 10a). The results show that a higher molar ratio of glycerol did not significantly improve the yield. This can be explained by the reaction temperature of 100 °C. At this temperature, the water molecules formed in the process are continuously evaporated, removing one of the products (H$_2$O) from the reaction medium. In this sense, the equilibrium is already driven towards product formation regardless of an excess of glycerol.

As shown in Figure 10b, reaction time plays a crucial role. While longer reaction times generally allow more cyclization and product formation, excessively long durations can lead to undesired byproducts or reagent degradation, ultimately decreasing yield. Therefore, it is

necessary to find a balance between reaction time and the formation of desired products to maximize the yield of acetals. Under the studied conditions, 10 min was sufficient to achieve an acetal yield of 80%.
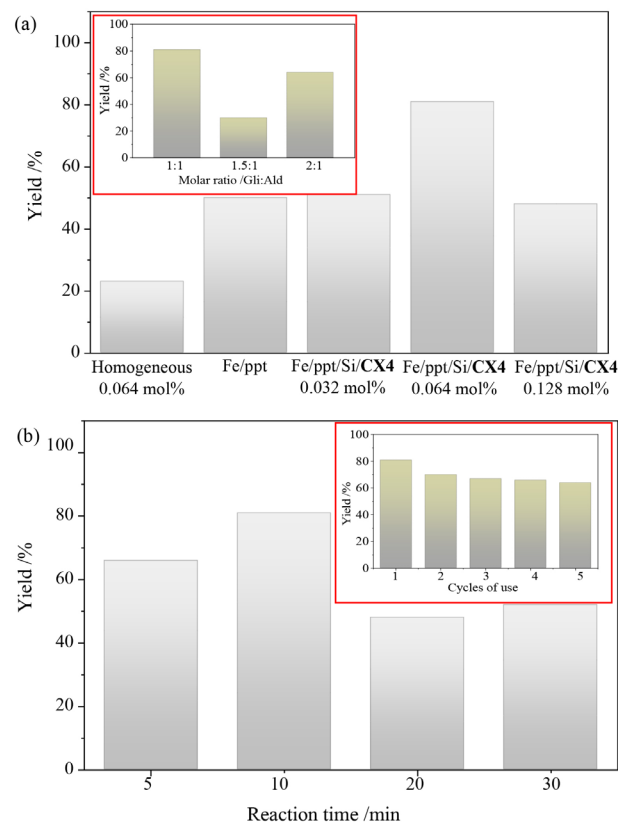

Figure 10. (a) Influence of the amount of catalyst (Fe/ppt/Si/CX4) in the reaction. The insert shows the effect of the molar ratio (glycerol/aldehyde) on yield using Fe/ppt/Si/CX4. (b) Effect of time on benzaldehyde acetalization reaction using Fe/ppt/Si/CX4. The insert shows the yield of five reaction cycles using Fe/ppt/Si/CX4. Reaction conditions: without solvent, 100 °C; MW, 10 min.

After verifying the high catalytic activity of Fe/ppt/Si/CX4, we evaluated its reusability over five cycles (insert in Figure 10b). Notably, the catalyst retains 83% of its initial activity between the first and fifth cycle. This slight decrease may be attributed to partial impregnation of glycerol on the catalyst surface. Nevertheless, the catalyst demonstrates good reusability in the context of heterogeneous catalysis.

The versatility of the Fe/ppt/Si/CX4 catalyst was further demonstrated by testing it in other reactions using aldehydes (**1a-1e**) containing a range of electron-donating and electron-withdrawing groups (Figure 11). This broad applicability suggests its potential for use with diverse substrates. Notably, the catalyst achieved high yields (or conversions) for several of the tested aldehydes, highlighting its effectiveness beyond the initial reaction studied.
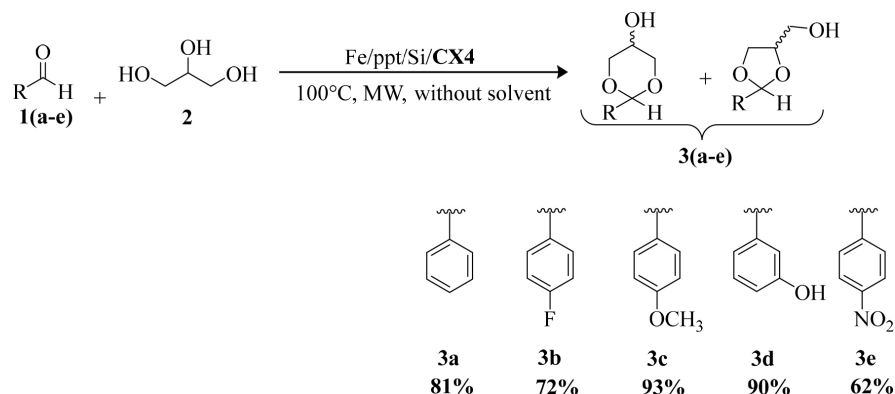
Figure 11. General scheme of the reaction with the optimized conditions and the aldehydes used to obtain the acetals.

The mixture of acetals with five- and six-membered rings obtained through acetalization reactions was characterized by ^{1}H NMR analysis (Figures S5-S9, SI section). Evaluation of the ^{1}H NMR spectra of these reaction mixtures (containing five- and six-membered rings) allowed for the calculation of the regio isomer ratio for each employed aldehyde (Figure 11). Detailed results are presented in Table 2.

Table 2. Regio isomer ratios of acetals determined by ^{1}H NMR (400 MHz,CDCl$_3$)

Product	Regio isomer ratios / %	
	Five members	Six members
3a	68	32
3b	62	38
3c	28	72
3d	33	67
3e	37	63

The formation of five and six-membered acetals in acetalization reactions is governed by an interplay between the thermodynamic stability of these rings and the steric characteristics of the reacting groups. Five-membered acetals are favored due to lower ring strain and greater resonance energy release than six-membered ones. Additionally, the more accessible approach of the reacting groups in five-membered ring formation contributes to their kinetically favored, faster reaction rate.[32]

This trend was evident in cases where the aromatic ring lacked substituent groups (**1a**) or featured a weak electron-donating group, such as fluorine (**1b**). On the other hand, electron-donating groups like methoxy (−OCH$_3$) or hydroxyl (−OH) on the aromatic ring of the aldehyde could stabilize carbocation formation, leading to the thermodynamically favored six-membered acetals. Interestingly, under our specific reaction conditions, the presence of a strong electron-withdrawing group (−NO$_2$) also led to the formation of

six-membered acetals. Therefore, neither the size nor the electronic pattern of the substituents in the aromatic ring solely explains the observed isomer ratio under our specific reaction conditions. Indeed, the distribution of five- and six-membered acetals derived from aromatic aldehydes differs not only depending on the volume or the electronic pattern of the substituents in the aromatic ring of the aldehydes but also on the characteristics of the catalyst and the reaction conditions used in the studies.[95,99,100]

Conclusions

This study describes the synthesis and application of magnetically recyclable Fe/ppt/Si/CX4 and Fe/pch/Si/CX4 composite catalysts, prepared directly using silica-coated magnetic nanoparticles and CX4, for the synthesis of acetals from various aldehydes and glycerol. Following the reactions, the catalysts were easily separated using an external magnet and maintained good catalytic activity in the subsequent five runs, experiencing only a modest 17% reduction in catalytic efficiency.

The optimal reaction conditions were achieved at a molar ratio of 1:1 (glycerol/aldehyde) with 0.064 mol% of the catalyst. The reactions were conducted without a solvent, utilizing microwave irradiation heating at 100 °C and atmospheric pressure. Notably, when Fe/ppt/Si/CX4 was employed as a catalyst, the yield surpassed 80%. This enhanced performance could be attributed to the synthesized specific structure and crystalline phases of iron oxide. The presence of α-FeOOH-like phases in this catalyst, absent in Fe/pch/Si/CX4, likely contributes to the superior catalytic activity.

Furthermore, SEM and TEM analyses revealed that Fe/ppt/Si/CX4 exhibited less homogeneous structures than those obtained through the Pechini method (Fe/pch/Si/CX4). This structural heterogeneity may partially explain the slight improvement in catalytic activity observed in Fe/ppt/Si/CX4 over Fe/pch/Si/CX4.

J. Braz. Chem. Soc. **2024**, *35*, 11, e-20240076

11 of 14

Furthermore, SEM and TEM analyses revealed that Fe/ppt/Si/CX4 exhibited less homogeneous structures than those obtained through the Pechini method (Fe/pch/Si/CX4). This heterogeneity in structure may partially explain the slight improvement in catalytic activity observed in Fe/ppt/Si/CX4 over Fe/pch/Si/CX4.

Supplementary Information

Supplementary information, including graphical representations, Mössbauer parameters for magnetic nanoparticles modified with silica and CX4, magnetization curves of the materials, FTIR spectra, TEM images of the catalysts, and ^{1}H NMR spectrum of the reaction products, is available free of charge at http://jbcs.sbq.org.br as PDF file.

Acknowledgments

Author Contributions

Carlos Henrique C. Zacchi was responsible for conceptualization, investigation, formal analysis, data curation, resources, writing; Sara S. Vieira for conceptualization, investigation, formal analysis, data curation, visualization, writing (original draft, review and editing); José D. Ardisson for investigation, formal analysis; Maria Helena Araujo for conceptualization, supervision, resources, writing review and editing; Ângelo de Fátima for conceptualization, supervision, resources, writing review and editing.

References

1. Agirre, I.; Güemez, M. B.; Ugarte, A.; Requies, J.; Barrio, V. L.; Cambra, J. F.; Arias, P. L.; *Fuel Process. Technol.* **2013**, *116*, 182. [Crossref]

2. Monteiro, M. R.; Kugelmeier, C. L.; Pinheiro, R. S.; Batalha, M. O.; da Silva César, A.; *Renewable Sustainable Energy Rev.* **2018**, *88*, 109. [Crossref]

3. Sánchez Faba, E. M.; Ferrero, G. O.; Dias, J. M.; Eimer, G. A.; *Appl. Catal., A.* **2020**, *604*, 117769. [Crossref]

4. Padula, I. D.; Santos, B. M. A.; Rodrigues, A. P. H.; Gastelois, P. L.; Mendes, I. M. C.; Portilho, M. F.; Oliveira, L. C. A.; Oliveira, C. C.; *Appl. Catal., A* **2020**, *606*, 117814. [Crossref]

5. Neves, P.; Russo, P. A.; Fernandes, A.; Antunes, M. M.; Farinha, J.; Pillinger, M.; Ribeiro, M. F.; Castanheiro, J. E.; Valente, A. A.; *Appl. Catal., A* **2014**, *487*, 148. [Crossref]

6. Rahaman, M. S.; Phung, T. K.; Hossain, M. A.; Chowdhury, E.; Tulaphol, S.; Lalvani, S. B.; O'Toole, M.; Willing, G. A.; Jasinski, J. B.; Crocker, M.; Sathitsuksanoh, N.; *Appl. Catal., A* **2020**, *592*, 117369. [Crossref]

7. Patel, A.; Pithadia, D.; *Appl. Catal., A* **2020**, *602*, 117729. [Crossref]

8. Saini, B.; Tathod, A. P.; Saxena, S. K.; Arumugam, S.; Viswanadham, N.; *ACS Sustainable Chem. Eng.* **2022**, *10*, 1172. [Crossref]

9. de Andrade, T. S.; Souza, M. M. V. M.; Manfro, R. L.; *Renewable Energy* **2020**, *160*, 919. [Crossref]

10. Ruy, A. D. S.; Alves, R. M. B.; Hewer, T. L. R.; Pontes, D. A.; Teixeira, L. S. G.; Pontes, L. A. M.; *Catal. Today* **2020**, *381*, 243. [Crossref]

11. Kostyniuk, A.; Bajec, D.; Djinović, P.; Likozar, B.; *Chem. Eng. J.* **2020**, *397*, 125430. [Crossref]

12. Zhao, S.; Wang, W. D.; Wang, L.; Wang, W.; Huang, J.; *J. Catal.* **2020**, *389*, 166. [Crossref]

13. Martín-Cabezuelo, R.; Vilariño-Feltrer, G.; Vallés-Lluch, A.; *Mater. Sci. Eng. C* **2021**, *119*, 111429. [Crossref]

14. Zanoni, A.; Gardoni, G.; Sponchioni, M.; Moscatelli, D.; *J. CO$_2$ Util.* **2020**, *40*, 101192. [Crossref]

15. Chagas, P.; Thibau, M. A.; Breder, S.; Souza, P. P.; Caldeira, G. S.; Portilho, M. F.; Castro, C. S.; Oliveira, L. C. A.; *Chem. Eng. J.* **2019**, *369*, 1102. [Crossref]

16. Dahdah, E.; Estephane, J.; Gennequin, C.; Aboukaïs, A.; Aouad, S.; Abi-Aad, E.; *J. Environ. Chem. Eng.* **2020**, *8*, 104228. [Crossref]

17. Dang, C.; Wang, H.; Yu, H.; Peng, F.; *Appl. Catal., A* **2017**, *533*, 9. [Crossref]

18. Zhou, D.; Wang, L.; Chen, X.; Wei, X.; Liang, J.; Tang, R.; Xu, Y.; *Chem. Eng. J.* **2020**, *401*, 126024. [Crossref]

19. Neto, A. B. S.; Oliveira, A. C.; Rodriguez-Castellón, E.; Campos, A. F.; Freire, P. T. C.; Sousa, F. F. F.; Filho, J. M.; Araujo, J. C. S.; Lang, R.; *Catal. Today* **2020**, *349*, 57. [Crossref]

20. Liu, J.; Zhang, Z.; Zhang, P.; Yang, B.; *Chem. Eng. J.* **2019**, *375*, 122037. [Crossref]

21. Bozkurt, Ö. D.; Bağlar, N.; Çelebi, S.; Uzun, A.; *Catal. Today* **2019**, *357*, 483. [Crossref]

22. Vannucci, J. A.; Legnoverde, M. S.; Dalla Costa, B. O.; Basaldella, E. I.; Nichio, N. N.; Pompeo, F.; *Mol. Catal.* **2022**, *528*, 112497. [Crossref]

23. Chen, L.; Nohair, B.; Kaliaguine, S.; *Appl. Catal., A* **2016**, *509*, 143. [Crossref]

12 of 14

J. Braz. Chem. Soc. **2024**, *35*, 11, e-20240076

24. Chen, L.; Nohair, B.; Zhao, D.; Kaliaguine, S.; *Appl. Catal., A* **2018**, *549*, 207. [Crossref]

25. Narkhede, N.; Patel, A.; *Appl. Catal., A* **2016**, *515*, 154. [Crossref]

26. Poly, S. S.; Jamil, M. A. R.; Touchy, A. S.; Yasumura, S.; Siddiki, S. M. A. H.; Toyao, T.; Maeno, Z.; Shimizu, K.; *Mol. Catal.* **2019**, *479*, 110608. [Crossref]

27. Oton, L. F.; Oliveira, A. C.; Tehuacanero-Cuapa, S.; Saraiva, G. D.; de Sousa, F. F.; Campos, A.; Duarte, G.; Bezerra, J. R.; *Mol. Catal.* **2020**, *496*, 111186. [Crossref]

28. Shen, C.; Li, Z.; Park, J. S.; Li, Z.; Li, C.; Hong, G. H.; Lee, J.; Moon, H.; Kim, J. M.; Jin, M.; *Mol. Catal.* **2022**, *520*, 112179. [Crossref]

29. Silva, P. H. R.; Gonçalves, V. L. C.; Mota, C. J. A.; *Bioresour. Technol.* **2010**, *101*, 6225. [Crossref]

30. Piasecki, A.; Sokołowski, A.; Burczyk, B.; Kotlewska, U.; *J. Am. Oil Chem. Soc.* **1997**, *74*, 33. [Crossref]

31. Climent, M. J.; Velty, A.; Corma, A.; *Green Chem.* **2002**, *4*, 565. [Crossref]

32. Deutsch, J.; Martin, A.; Lieske, H.; *J. Catal.* **2007**, *245*, 428. [Crossref]

33. Serafim, H.; Fonseca, I. M.; Ramos, A. M.; Vital, J.; Castanheiro, J. E.; *Chem. Eng. J.* **2011**, *178*, 291. [Crossref]

34. Pawar, R. R.; Jadhav, S. V.; Bajaj, H. C.; *Chem. Eng. J.* **2014**, *235*, 61. [Crossref]

35. Sadjadi, S.; Tarighi, S.; Moussavi, N. S.; Ahadi, N.; *J. Mol. Struct.* **2022**, *1256*, 132556. [Crossref]

36. Pinheiro, A. L. G.; do Carmo, J. V. C.; Carvalho, D. C.; Oliveira, A. C.; Rodríguez-Castellón, E.; Tehuacanero-Cuapa, S.; Otubo, L.; Lang, R.; *Fuel Process. Technol.* **2019**, *184*, 45. [Crossref]

37. Khayoon, M. S.; Hameed, B. H.; *Appl. Catal., A* **2013**, *464-465*, 191. [Crossref]

38. Castanheiro, J. E.; Vital, J.; Fonseca, I. M.; Ramos, A. M.; *Catal. Today* **2022**, *384-386*, 2. [Crossref]

39. Wang, B.; Shen, Y.; Sun, J.; Xu, F.; Sun, R.; *RSC Adv.* **2014**, *4*, 18917. [Crossref]

40. Teixeira, A. P. C.; Tristão, J. C.; Araujo, M. H.; Oliveira, L. C. A.; Moura, F. C. C.; Ardisson, J. D.; Amorim, C. C.; Lago, R. M.; *J. Braz. Chem. Soc.* **2012**, *23*, 1579. [Crossref]

41. Oliveira, L. C. A.; Fabris, J. D.; Pereira, M. C.; *Quim. Nova* **2013**, *36*, 123. [Crossref]

42. Kumar, P.; Tomar, V.; Kumar, D.; Joshi, R. K.; Nemiwal, M.; *Tetrahedron* **2022**, *106-107*, 132641. [Crossref]

43. Tajbakhsh, M.; Mazhari, F.; Nirouei, N.; *Res. Chem. Intermed.* **2024**, *50*, 1287. [Crossref]

44. Maleki, B.; Reiser, O.; Esmaeilnezhad, E.; Choi, H. J.; *Polyhedron* **2019**, *162*, 129. [Crossref]

45. Maleki, A.; Rahimi, J.; Hajizadeh, Z.; Niksefat, M.; *J. Organomet. Chem.* **2019**, *881*, 58. [Crossref]

46. Sharma, R. K.; Yadav, M.; Gawande, M. B.; K. Sharma, R.; Gawande, M. B. In *Ferrites and Ferrates: Chemistry and Applications in Sustainable Energy and Environmental Remediation*; Sharma, V. K.; Doong, R.; Kim, H.; Varma, R. S.; Dionysiou, D. D., eds.; American Chemical Society: Washington, DC, 2016. [Crossref]

47. Zacchi, C. H. C.; Vieira, S. S.; Ardisson, J. D.; Araujo, M. H.; de Fátima, Â.; *J. Saudi Chem. Soc.* **2019**, *23*, 1060. [Crossref]

48. Simoes, J. B.; da Silva, D. L.; de Fatima, A.; Fernandes, S. A.; *Curr. Org. Chem.* **2012**, *16*, 949. [Crossref]

49. Ben-Ishay, M. L.; Gedanken, A.; *Langmuir* **2007**, *23*, 5238. [Crossref]

50. Castro, G. A. D.; Santos, A. L. Q.; Sathicq, Á. G.; Palermo, V.; Romanelli, G. P.; Fernandes, S. A.; *React. Chem. Eng.* **2022**, *7*, 2132. [Crossref]

51. Castro, G. A. D.; Batista, R. C.; de Sousa, R. C. S.; Carneiro, A. C. O.; Fernandes, S. A.; *React. Chem. Eng.* **2023**, *8*, 1969. [Crossref]

52. Castro, G. A. D.; Fernandes, S. A.; *Catal. Lett.* **2023**, *153*, 984. [Crossref]

53. Supattarasakda, K.; Petcharoen, K.; Permpool, T.; Sirivat, A.; Lerdwijitjarud, W.; *Powder Technol.* **2013**, *249*, 353. [Crossref]

54. Primc, D.; Belec, B.; Makovec, D.; *J. Nanoparticle Res.* **2016**, *18*, 64. [Crossref]

55. Lassoued, A.; Dkhil, B.; Gadri, A.; Ammar, S.; *Results Phys.* **2017**, *7*, 3007. [Crossref]

56. LaGrow, A. P.; Besenhard, M. O.; Hodzic, A.; Sergides, A.; Bogart, L. K.; Gavriilidis, A.; Thanh, N. T. K.; *Nanoscale* **2019**, *11*, 6620. [Crossref]

57. de Souza, T. E.; Mesquita, A.; de Zevallos, A. O.; Béron, F.; Pirota, K. R.; Neves, P. P.; Doriguetto, A. C.; de Carvalho, H. B.; *J. Phys. Chem. C* **2013**, *117*, 13252. [Crossref]

58. Rudisill, S. G.; Hein, N. M.; Terzic, D.; Stein, A.; *Chem. Mater.* **2013**, *25*, 745. [Crossref]

59. Suppiah, D. D.; Abd Hamid, S. B.; *J. Magn. Magn. Mater.* **2016**, *414*, 204. [Crossref]

60. Sayin, S.; Ozcan, F.; Yilmaz, M.; *J. Hazard. Mater.* **2010**, *178*, 312. [Crossref]

61. Simões, J. B.; de Fátima, Â.; Sabino, A. A.; de Aquino, F. J. T.; da Silva, D. L.; Barbosa, L. C. A.; Fernandes, S. A.; *Org. Biomol. Chem.* **2013**, *11*, 5069. [Crossref]

62. da Silva, D. L.; Terra, B. S.; Lage, M. R.; Ruiz, A. L. T. G.; da Silva, C. C.; de Carvalho, J. E.; Carneiro, J. W. M.; Martins, F. T.; Fernades, S. A.; de Fátima, Â.; *Org. Biomol. Chem.* **2015**, *13*, 3280. [Crossref]

63. Sayin, S.; Ozcan, F.; Yilmaz, M.; Tor, A.; Memon, S.; Cengeloglu, Y.; *Clean: Soil, Air, Water* **2010**, *38*, 639. [Crossref]

64. Cuenya, B. R.; Behafarid, F.; *Surf. Sci. Rep.* **2015**, *70*, 135. [Crossref]

65. Amos-Tautua, B. M.; Fakayode, O. J.; Songca, S. P.; Oluwafemi, O. S.; *Nano-Struct. Nano-Objects* **2020**, *23*, 100480. [Crossref]

66. da Silva, D. L.; Fernandes, S. A.; Sabino, A. A.; de Fátima, Â.; *Tetrahedron Lett.* **2011**, *52*, 6328. [Crossref]

J. Braz. Chem. Soc. **2024**, *35*, 11, e-20240076

13 of 14

67. Abranches, P. A. D. S.; De Paiva, W. F.; De Fátima, Â.; Martins, F. T.; Fernandes, S. A.; *J. Org. Chem.* **2018**, *83*, 1761. [Crossref]

68. Cano, I.; Martin, C.; Fernandes, J. A.; Lodge, R. W.; Dupont, J.; Casado-Carmona, F. A.; Lucena, R.; Cardenas, S.; Sans, V.; de Pedro, I.; *Appl. Catal., B* **2020**, *260*, 118110. [Crossref]

69. Mobinikhaledi, A.; Khajeh-Amiri, A.; *React. Kinet., Mech. Catal.* **2014**, *112*, 131. [Crossref]

70. Leone, V. O.; Pereira, M. C.; Aquino, S. F.; Oliveira, L. C. A.; Correa, S.; Ramalho, T. C.; Gurgel, L. V. A.; Silva, A. C.; *New J. Chem.* **2018**, *42*, 437. [Crossref]

71. Nadar, A.; Banerjee, A. M.; Pai, M. R.; Meena, S. S.; Pai, R. V.; Tewari, R.; Yusuf, S. M.; Tripathi, A. K.; Bharadwaj, S. R.; *Appl. Catal., B* **2017**, *217*, 154. [Crossref]

72. Momma, K.; Izumi, F.; *J. Appl. Crystallogr.* **2011**, *44*, 1272. [Crossref]

73. Merkys, A.; Vaitkus, A.; Butkus, J.; Okulič-Kazarinas, M.; Kairys, V.; Gražulis, S.; *J. Appl. Crystallogr.* **2016**, *49*, 292. [Crossref]

74. Cornell, R. M.; Schwertmann, U.; *The Iron Oxides: Structure, Properties, Reactions, Occurrences and Uses*, 2nd ed.; Wiley: New Jersey, 2006. [Link] accessed in April 2024

75. Antarnusa, G.; Nene, A.; Umam, R.; Swastika, P. E.; *Nano-Struct. Nano-Objects* **2024**, *38*, 101123. [Crossref]

76. Chen, F.; Liu, R.; Xiao, S.; Zhang, C.; *Mater. Res. Bull.* **2014**, *55*, 38. [Crossref]

77. Zhang, W.; Shen, F.; Hong, R.; *Particuology* **2011**, *9*, 179. [Crossref]

78. Li, C.; Wei, Y.; Liivat, A.; Zhu, Y.; Zhu, J.; *Mater. Lett.* **2013**, *107*, 23. [Crossref]

79. Rostami, A.; Atashkar, B.; Gholami, H.; *Catal. Commun.* **2013**, *37*, 69. [Crossref]

80. Rajabzadeh, M.; Eshghi, H.; Khalifeh, R.; Bakavoli, M.; *Appl. Organomet. Chem.* **2018**, *32*, e4052. [Crossref]

81. Safari, J.; Zarnegar, Z.; Heydarian, M.; *Bull. Chem. Soc. Jpn.* **2012**, *85*, 1332. [Crossref]

82. Bhosale, M. A.; Ummineni, D.; Sasaki, T.; Nishio-Hamane, D.; Bhanage, B. M.; *J. Mol. Catal. A: Chem.* **2015**, *404-405*, 8. [Crossref]

83. Zarghani, M.; Akhlaghinia, B.; *RSC Adv.* **2016**, *6*, 38592. [Crossref]

84. Otokesh, S.; Kolvari, E.; Amoozadeh, A.; Koukabi, N.; *RSC Adv.* **2015**, *5*, 53749. [Crossref]

85. Beygzadeh, M.; Alizadeh, A.; Khodaei, M. M.; Kordestani, D.; *Catal. Commun.* **2013**, *32*, 86. [Crossref]

86. Alizadeh, A.; Khodaei, M. M.; Beygzadeh, M.; Kordestani, D.; Feyzi, M.; *Bull. Korean Chem. Soc.* **2012**, *33*, 2546. [Crossref]

87. Sobhani, S.; Ghasemzadeh, M. S.; Honarmand, M.; *Catal. Lett.* **2014**, *144*, 1515. [Crossref]

88. Sayin, S.; Yilmaz, M.; *J. Chem. Eng. Data* **2011**, *56*, 2020. [Crossref]

89. Sheykhan, M.; Yahyazadeh, A.; Ramezani, L.; *Mol. Catal.* **2017**, *435*, 166. [Crossref]

90. Shmygleva, L.; Slesarenko, N.; Chernyak, A.; Sanginov, E.; Karelin, A.; Pisareva, A.; Pisarev, R.; Dobrovolsky, Y.; *Int. J. Electrochem. Sci.* **2017**, *12*, 4056. [Crossref]

91. Narkhede, N.; Uttam, B.; Kandi, R.; Rao, C. P.; *ACS Omega* **2018**, *3*, 229. [Crossref]

92. Shiri, L.; Zarei, S.; Kazemi, M.; Sheikh, D.; *Appl. Organomet. Chem.* **2018**, *32*, e3938. [Crossref]

93. Kosmulski, M.; Durand-Vidal, S.; Mączka, E.; Rosenholm, J. B.; *J. Colloid Interface Sci.* **2004**, *271*, 261. [Crossref]

94. Ovejero, J. G.; Garcia, M. A.; Herrasti, P.; *Molecules* **2021**, *26*, 6943. [Crossref]

95. Umbarkar, S. B.; Kotbagi, T. V.; Biradar, A. V.; Pasricha, R.; Chanale, J.; Dongare, M. K.; Mamede, A. S.; Lancelot, C.; Payen, E.; *J. Mol. Catal. A: Chem.* **2009**, *310*, 150. [Crossref]

96. Chandrasekhar, S.; *Chem. Soc. Rev.* **1987**, *16*, 313. [Crossref]

97. Mota, C. J. A.; da Silva, C. X. A.; Gonçalves, V. L. C.; *Quim. Nova* **2009**, *32*, 639. [Crossref]

98. de Paiva, W. F.; Braga, I. B.; de Assis, J. V.; Castañeda, S. M. B.; Sathicq, Á. G.; Palermo, V.; Romanelli, G. P.; Natalino, R.; da Silva, M. J.; Martins, F. T.; de Carvalho, G. S. G.; Amarante, G. W.; Fernandes, S. A.; *Tetrahedron* **2019**, *75*, 3740. [Crossref]

99. Trifoi, A. R.; Agachi, P. Ş.; Pap, T.; *Renew. Sustainable Energy Rev.* **2016**, *62*, 804. [Crossref]

100. Armylisas, A. H. N.; Yeong, S. K.; Maznee, T. I. T. N.; Hoong, S. S.; *Chem. Full* **2021**, *6*, 256. [Crossref]